Advances in Water Resources 62 (2013) 511–519

Contents lists available at SciVerse ScienceDirect

Advances in Water Resources

journal homepage: www.elsevier.com/locate/advwatres

Dynamics of convective dissolution from a migrating current of carbon dioxide

Juan J. Hidalgo [a,b], Christopher W. MacMinn [c], Ruben Juanes [a,*]

[a] Massachusetts Institute of Technology, Cambridge, MA, USA
[b] Institute for Environmental Assessment and Water Research, Spanish National Research Council, Barcelona, Spain
[c] Yale University, New Haven, CT, USA

ARTICLE INFO

Article history:
Available online 4 July 2013

Keywords:
CO_2 sequestration
Gravity current
Convective dissolution
Sharp interface model
Upscaling

ABSTRACT

During geologic storage of carbon dioxide (CO_2), trapping of the buoyant CO_2 after injection is essential in order to minimize the risk of leakage into shallower formations through a fracture or abandoned well. Models for the subsurface behavior of the CO_2 are useful for the design, implementation, and long-term monitoring of injection sites, but traditional reservoir-simulation tools are currently unable to resolve the impact of small-scale trapping processes on fluid flow at the scale of a geologic basin. Here, we study the impact of solubility trapping from convective dissolution on the up-dip migration of a buoyant gravity current in a sloping aquifer. To do so, we conduct high-resolution numerical simulations of the gravity current that forms from a pair of miscible analogue fluids. Our simulations fully resolve the dense, sinking fingers that drive the convective dissolution process. We analyze the dynamics of the dissolution flux along the moving CO_2–brine interface, including its decay as dissolved buoyant fluid accumulates beneath the buoyant current. We show that the dynamics of the dissolution flux and the macroscopic features of the migrating current can be captured with an upscaled sharp-interface model.

1. Introduction

The injection of carbon dioxide (CO_2) into deep saline aquifers is a promising tool for reducing anthropogenic CO_2 emissions [1–4]. After injection, the buoyant CO_2 will spread and migrate laterally as a gravity current relative to the denser ambient brine, increasing the risk of leakage into shallower formations through fractures, outcrops, or abandoned wells.

One mechanism that acts to arrest and securely trap the migrating CO_2 is dissolution of CO_2 into the brine [5]. Dissolved CO_2 is considered trapped because brine with dissolved CO_2 is denser than the ambient brine, and sinks to the bottom of the aquifer. In addition to providing storage security by hindering the return of the CO_2 to the atmosphere, this sinking fluid triggers a hydrodynamic fingering instability that drives convection in the brine and greatly enhances the rate of CO_2 dissolution [6–9].

Although this process of convective dissolution is expected to play a major role in limiting CO_2 migration and accelerating CO_2 trapping [4], the interaction of convective dissolution with a migrating gravity current remains poorly understood. This is due primarily to the disparity in scales between the long, thin gravity current and the details of the fingering instability. Resolving these simultaneously has proven challenging for traditional reservoir simulation tools [10]. Upscaled theoretical models [11,12] and laboratory experiments [13,14] have recently provided some macroscopic insights, but by design these capture only the averaged dynamics of the dissolution process.

Here, we study the impact of convective dissolution on the migration of a buoyant gravity current in a sloping aquifer by conducting high-resolution numerical simulations of a pair of miscible analogue fluids. Our simulations fully resolve the small-scale features of the convective dissolution process. We define an average dissolution flux and use it to study the dynamic interactions of the fingering instability with the migrating current. We then compare these results with the predictions of an upscaled theoretical model to investigate the degree to which this simple model can capture the macroscopic features of the migrating current.

2. Analogue fluids

For simplicity, and to focus on the role of convective dissolution, we neglect capillarity and assume that the two fluids are perfectly miscible. We adopt constitutive laws for density and viscosity that are inspired by a pair of miscible analogue fluids that have been used to study this problem experimentally [15,16,13,14]. This system captures three key features of the CO_2-brine system: (1) a density contrast that stratifies the pure fluids and drives the migration

* Corresponding author.
E-mail addresses: jhidalgo@mit.edu (J.J. Hidalgo), christopher.macminn@yale.edu (C.W. MacMinn), juanes@mit.edu (R. Juanes).

0309-1708/$ - see front matter © 2013 Elsevier Ltd. All rights reserved.
http://dx.doi.org/10.1016/j.advwatres.2013.06.013

of the gravity current, (2) an intermediate density maximum that triggers and drives convective dissolution (discussed below), and (3) a viscosity contrast between the pure fluids that influences the shape and propagation speed of the gravity current.

We write the dimensionless density ρ and viscosity μ as functions of the local concentration c of the buoyant fluid. We scale the concentration c by the solubility so that $c \in [0, 1]$. Since the analogue fluids have different densities ($\rho(c = 1) < \rho(c = 0)$), the buoyant one will "float" and migrate above the denser one. Since they are perfectly miscible, they will be separated by a transition zone that forms and grows through diffusion, and within which the local concentration transitions from $c = 0$ to $c = 1$ and the local density and viscosity vary accordingly.

To trigger convective dissolution, the essential feature of the density law is that it must be a non-monotonic function of concentration with an intermediate maximum (Fig. 1). This shape introduces a neutral concentration $c = c_n$ for which the density of the mixture is equal to the density of the ambient fluid. Fluid with concentration $c > c_n$ (*i.e.*, to the right of c_n) is less dense than the ambient and tends to float, whereas fluid with concentration $c < c_n$ (*i.e.*, to the left of c_n) is *denser* than the ambient and tends to sink. The contour of neutral concentration within the transition zone therefore emerges as a natural "interface" between buoyant and sinking fluids: the fluid above is buoyant and stably stratified (density decreasing as concentration increases from $c = c_n$ to $c = 1$), the fluid below is dense and unstably stratified (density decreasing as concentration decreases from $c = c_n$ to $c = 0$), and diffusion continuously transfers fluid from the stable region to the unstable region.

The concentration $c = c_m$ at which the density maximum occurs plays the role of a solubility in this system since the density of the underlying fluid increases toward this value as dissolved buoyant fluid accumulates. Convective dissolution stops entirely when diffusion at the interface is no longer able to generate a mixture that is denser than the fluid below it.

To make the density law dimensionless, we shift it by the brine density and scale it by the height of the density maximum so that the dimensionless brine density is always $\rho(c = 0) = 0$ and the dimensionless density maximum is always $\rho(c = c_m) = 1$. We represent the density law with a polynomial of degree three, $\rho(c) = 6.19c^3 - 17.86c^2 + 8.07c$, which has neutral concentration $c_n = 0.56$, a density maximum at $c_m = 0.26$, and a dimensionless CO_2 density of $\rho(c = 1) = -3.6$. This density law is qualitatively and quantitatively similar to the true density law for mixtures of propylene glycol ($c = 0$, brine analogue) and water ($c = 1$, CO_2 analogue) [16].

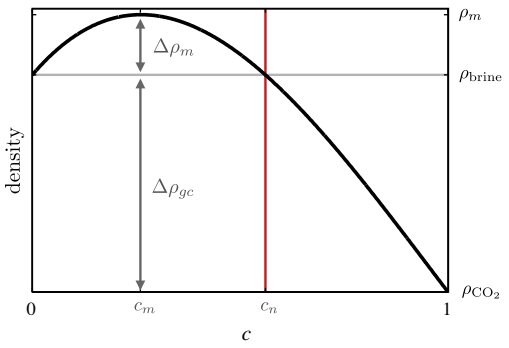

Fig. 1. Non-monotonic density law (dimensional) inspired by miscible analogue fluids [15,16]. The density has a maximum at $c = c_m$. The contour of neutral concentration $c = c_n$ (red line) acts as an interface: mixtures with $c < c_n$ (left of the red line) are denser than the ambient brine and will sink, whereas those with $c > c_n$ (right of the red line) are buoyant relative to the ambient brine and will rise. $\Delta\rho_m$ is the characteristic density difference that drives convective dissolution and $\Delta\rho_{gc}$ is the one that drives the migration of the buoyant gravity current. (For interpretation of the references to color in this figure legend, the reader is referred to the web version of this article.)

We choose an exponential constitutive law for the dimensionless viscosity, $\mu(c) = \exp[R(c_m - c)]$, where we have scaled $\mu(c)$ by characteristic viscosity μ_m so that $\mu(c = c_m = 0.26) = 1$. The parameter $R = \ln \mathcal{M}$, where $\mathcal{M} = \mu_{\text{brine}}/\mu_{CO_2} = \mu(c = 0)/\mu(c = 1)$ is the mobility ratio. This viscosity law is qualitatively and quantitatively similar to the true viscosity law for mixtures of propylene glycol and water for $R \approx 3.7$ [16].

Since these analogue fluids are perfectly miscible, our results do not incorporate the various impacts of capillarity, including residual trapping, the development of a capillary fringe, and capillary pressure hysteresis. The absence of capillarity is a limitation in the sense that these analogue fluids cannot capture every aspect of the CO_2–brine system, but it is also an advantage in the sense that it allows us to isolate and study convective dissolution as a transport process without these additional complications [15,16,13,14].

Capillarity may impact the dynamics of the gravity current. For example, the gravity current will shrink due to residual trapping along its trailing edge [17–19]. The formation of a capillary fringe between the CO_2 and the brine may change the shape and reduce the propagation speed of the gravity current [20–22]. Capillary pressure hysteresis may also reduce the propagation speed of the gravity current and even arrest its migration [23,24]. All of these effects can be incorporated into upscaled models for CO_2 migration, but incorporating them into our 2D simulations is less straightforward. These effects would impact the total dissolution rate by changing the length of the "interface" between the two fluids, and by reducing the amount of ambient fluid available for "storing" dissolved CO_2. However, we would not expect them to change the dynamic interactions of migration and dissolution as described here.

Capillarity may also have a quantitative impact on the onset and subsequent rate of convective dissolution [25–27]. These effects have never been studied experimentally and are not well understood, but we expect the same qualitative behavior of the dissolution flux (diffusion, onset, convection). Although miscible analogue fluid systems may feature quantitatively different fluxes, they are useful for studying the dynamics of the dissolution flux and its impact on migration.

3. Mathematical model

We consider a two-dimensional aquifer in the x–z plane, with dimensional length L_x and uniform dimensional thickness L_z. The aquifer is tilted by an angle θ relative to horizontal. This can be viewed as a cross-section of a sedimentary basin taken perpendicular to a line-drive array of injection wells [28,4]. We assume that the aquifer is homogeneous and with isotropic permeability.

We use the classical model for incompressible fluid flow and advective–dispersive mass transport under the Boussinesq approximation, modeling hydrodynamic dispersion as a Fickian process with a velocity-independent diffusion–dispersion coefficient. The governing equations for this model in dimensionless form are [29]

$$\nabla \cdot \mathbf{u} = 0, \tag{1}$$

$$\mathbf{u} = -\frac{1}{\mu(c)}\left(\nabla p - \rho(c)\hat{\mathbf{e}}_g\right), \tag{2}$$

$$\frac{\partial c}{\partial t} = -\mathbf{u} \cdot \nabla c + \frac{1}{\text{Ra}}\nabla^2 c, \tag{3}$$

where p is the scaled pressure deviation from a hydrostatic datum, $\mathbf{u}$ is the scaled Darcy velocity, and $\hat{\mathbf{e}}_g = (-\sin\theta, -\cos\theta)$ is the unit vector in the direction of gravity. $\rho(c)$ and $\mu(c)$ are the dimensionless

density and viscosity as functions of the scaled concentration c, as discussed in Section 2. The Rayleigh number Ra is given by

$$\mathrm{Ra} = \frac{\Delta\rho_m g k L_z}{\phi D_m \mu_m}, \tag{4}$$

where g is the body force per unit mass due to gravity, ϕ is porosity, k is the aquifer permeability, D_m is the diffusion–dispersion coefficient, $\Delta\rho_m$ is the characteristic density difference driving convective dissolution, and μ_m is the characteristic viscosity. We write Eqs. (1)–(3) in dimensional form and give the complete details of the scaling with which we make them dimensionless in Appendix A.

The behavior of a buoyant gravity current is then completely characterized by Eqs. (1)–(3), the value of Ra, the constitutive laws $\rho(c)$ and $\mu(c)$, and appropriate initial and boundary conditions.

To study convective dissolution from a gravity current, we solve Eqs. (1)–(3) numerically in a rectangular domain of dimensionless height 1 and length $A = L_x/L_z = 20$. We discretize the equations for flow (Eqs. (1) and (2)) and transport (Eq. (3)) in space using 2nd-order finite volumes and 6th-order compact finite differences (4th order for boundary conditions), respectively, in a domain of 10000×500 grid blocks (see Appendix B). We evolve this system in time using an explicit 3rd-order Runge–Kutta scheme.

We prescribe the pressure along the right boundary and take the other boundaries to be impervious. We then write the dimensionless boundary conditions as

$$p = 0 \text{ at } x = A, \tag{5}$$

$$\mathbf{u}\cdot\mathbf{n} = 0 \text{ elsewhere} \tag{6}$$

for flow, and

$$\nabla c \cdot \mathbf{n} = 0 \tag{7}$$

for transport.

Initially, the region $x \leqslant 4$ is filled with CO_2.We do not add any perturbation to trigger the instability, which is started by numerical errors [30]. A sequence of snapshots from a typical simulation is shown in Fig. 2. These results are qualitatively similar to the fingering patterns observed in experiments using water and propylene glycol, although those fluids have a much higher value of R $\sim$ 3.7 [16,14].

Reported values of the Rayleigh number in real CO_2 sequestration scenarios range over several orders of magnitude, from as low as 100 in thin, low-permeability aquifers to as high as 10^5 in thick, high-permeability aquifers. Our results here target the middle of this range, Ra $\sim$ 5000, to explore the limit in which diffusion is still important and to show the convergence of the dissolution behavior for Ra $>$ 5000.

The mobility ratio for a real CO_2–brine system is $\mathcal{M} \approx 5$–12 or $R \approx 1.5$–2.5 [4], which is somewhat higher than the values used here ($R = 0$ and 1). The mobility ratio has a direct impact on the dynamics of the gravity current, which is longer, thinner, and more strongly tongued for larger R [18,31]. It also has a weak impact on the magnitude of the dissolution flux, as shown in [32] and in the present work (Fig. 5(d)).

The aspect ratio of the initial condition is the width of the initial rectangle of buoyant fluid relative to the width of the thickness the aquifer, which we take here to be 4. This is a realistic value for carbon sequestration, although field values can range from an order of magnitude smaller (~ 0.4) to an order of magnitude larger (~ 40) depending on the thickness of the aquifer and the volume of CO_2 injected [4].

4. Effect of dissolution on CO_2 migration

We quantify the evolution of the buoyant current with four macroscopic quantities: its mass, its length, the total dissolution rate of CO_2 into the brine, and the average dissolution flux per unit length of the current. These quantities characterize the spreading and migration of the current and the effectiveness of solubility trapping, which have implications for planning and risk assessment [33,34].

The dissolution flux between two miscible fluids must be defined with care since there is no true interface across which mass is transferred. Instead, there is an initial concentration distribution that homogenizes as mixing progresses. Although the natural characterization for such a system is through the evolution of the mean scalar dissipation rate [32], it is useful in practice to define a dissolution flux. Here, we define the dissolution flux via the non-monotonic behavior of fluid density with concentration. Since mixtures with concentration $c = c_n$ are neutrally buoyant relative to the ambient fluid, this concentration can be used to define a *neutral contour* separating the buoyant, mobile CO_2 ($c \geqslant c_n$) from the dense brine with dissolved CO_2 ($c < c_n$; Fig. 1). This is an unstable equilibrium point and any perturbation of concentration causes significant buoyancy forces that trigger convection. To define the dissolution flux, we first compute the mass of buoyant fluid as $M_b(t) = \int_{\Omega_b(t)} c\,\mathrm{d}\Omega, \Omega_b(t) := \{(x,z)\,|\,c(x,z,t) > c_n\}$ (Fig. 3(a)). We then define the *total dissolution rate* as $-\mathrm{d}M_b/\mathrm{d}t$ (Fig. 3(b)). By dividing this quantity by the length of CO_2–brine interface, which we mea-

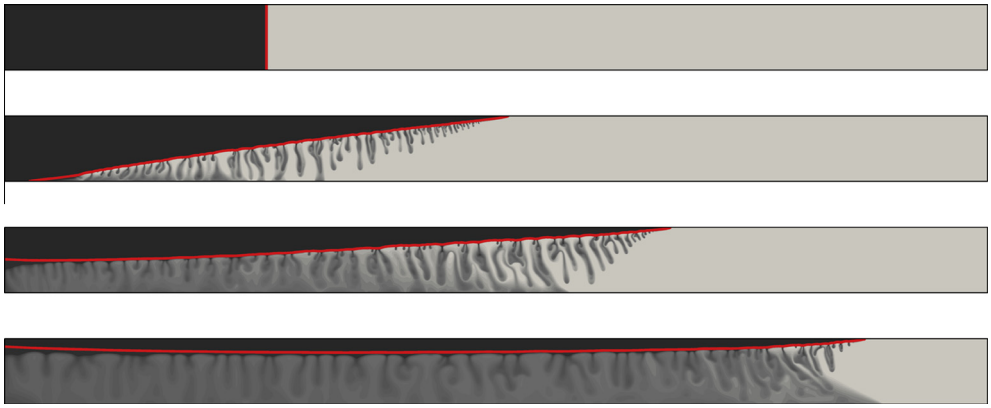

Fig. 2. Sequence of snapshots from a high-resolution simulation of convective dissolution from a buoyant current in a sloping aquifer for Ra = 5000, $R = 1$, and $\theta = 2.5^\circ$ (not shown) at dimensionless times 0, 3, 9, and 27. The domain extends to $x = 20$, but only $0 \leqslant x \leqslant 15$ is shown here. The red line marks the contour of neutrally buoyant concentration $c = c_n$, which separates the buoyant current from the sinking fluid (Fig. 1). (For interpretation of the references to color in this figure legend, the reader is referred to the web version of this article.)

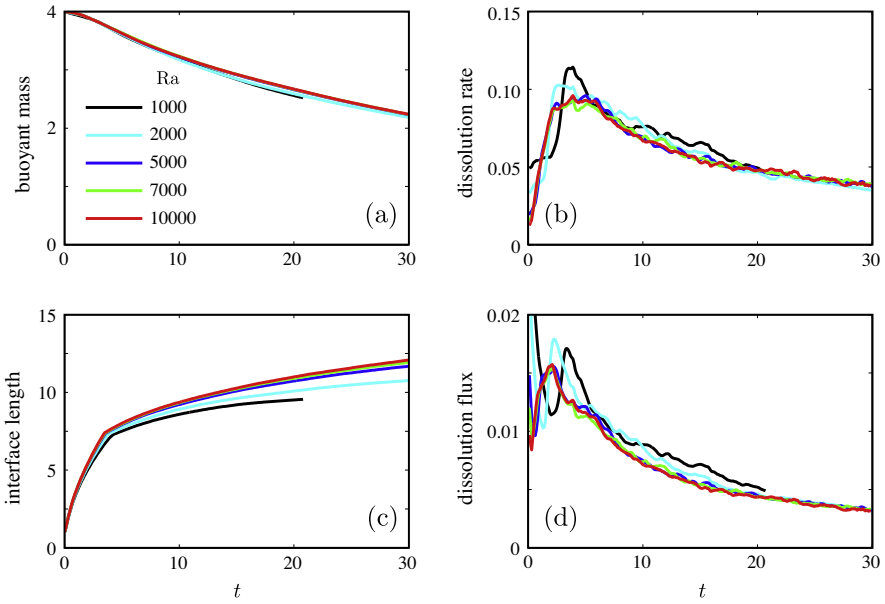

Fig. 3. We characterize the dynamics of convective dissolution from a migrating gravity current with the time evolution of four macroscopic quantities: (a) the remaining buoyant mass, $M_b(t)$, (b) the total dissolution rate, $-\mathrm{d}M_b/\mathrm{d}t$, (c) the length of the CO_2-brine interface, $L(t)$, measured as the length of the neutral contour, and (d) the average dissolution flux per unit interface length, $-(1/L)\mathrm{d}M_b/\mathrm{d}t$. Results shown here are for $R = 0$, $\theta = 2.5^\circ$, and several values of Ra, as indicated.

sure as the length of the neutral contour (Fig. 3(c)), we obtain the *average dissolution flux* (Fig. 3(d)).

Both the total dissolution rate and the average dissolution flux evolve as the buoyant current migrates (Fig. 3(b) and (d)). Much like for a stationary layer of CO_2 dissolving into brine [9,30,15,16,32,35], we distinguish three distinct regimes in convective dissolution from the migrating current: a diffusive regime at early times, a constant-flux regime during intermediate times, and a decay at late times. The early-time evolution of the gravity current in this system is a classical lock exchange, where an initially vertical interface between a buoyant fluid and a dense fluid evolves by tilting and stretching (here with the added complication of convective dissolution). The classical sharp-interface model for lock exchange predicts that the length of the interface will grow proportional to $t^{1/2}$ [36]. This regime ceases here when the left-traveling edge of the interface hits the left boundary of the domain, at which point the dynamics of the interface change suddenly as the gravity current detaches from the bottom of the aquifer and enters a migration-dominated regime (Fig. 3(c)) [37]. Both the dissolution rate and dissolution flux are small at early times as the CO_2–brine interface tilts from its initial, vertical orientation and diffusion–dispersion dominates. After the onset of convection ($t \approx 1$), the dissolution flux becomes roughly constant ($t \approx 1$–4), as expected for a stationary layer, and the growth of the interface slows down. Before the fingers interact significantly with the bottom boundary, our computed dissolution flux exhibits the same qualitative behavior as has been observed previously for dissolution of a stationary layer [30,38,32]. However, our flux differs quantitatively from these previous measurements. This is expected since the value of the flux has been shown to depend strongly on the concentration at which the density maximum occurs [32], and also on the nature of the boundary condition at the boundary where dissolution occurs (here across a moving interface between two miscible fluids *vs.* across a rigid boundary with prescribed concentration) [32,26]. The total dissolution rate grows strongly during this period since the interface length grows rapidly (Fig. 3(c)) while the flux remains roughly constant. At later times ($t > 5$), the accumulation of dissolved CO_2 under the leftmost part of the current begins to suppress further convective dissolution there and the average dissolution flux begins to decay (Fig. 3(d)) [13,35]. The total dissolution rate also decays (Fig. 3(b)) even though the length of the interface continues to increase (Fig. 3(c)), reflecting the fact that the accumulation of dissolved CO_2 is suppressing convective dissolution along a progressively larger fraction of the interface (Fig. 2).

As Ra increases, we find that the dynamics of this process converge to a common high-Ra limit, indicating that relevant macroscopic quantities are independent of Ra for Ra $\approx$ 5000 and higher [32]. We therefore fix Ra = 5000 in what follows.

5. Upscaled model

We now consider the extent to which the dynamics of convective dissolution from a migrating gravity current can be captured by a simple upscaled model. Such models have recently been used to develop insight into the physics of CO_2 migration and trapping [12,18,19,31,37,39–41].

We have elsewhere presented an upscaled model for the migration and trapping of a buoyant current of CO_2 in a sloping aquifer [12]. The model adopts the sharp-interface approximation, assumes vertical flow equilibrium, and neglects capillarity. The model accounts for residual trapping, but we ignore this here for simplicity. Here, we extend the model to include the slumping of the CO_2-rich brine layer against the bottom of the aquifer as in [13]. We outline the derivation of this model in Appendix C.

The model incorporates convective dissolution as a constant flux of CO_2 per unit length of CO_2–brine interface [30,38,15,16,32]. This rate will decay as dissolved CO_2 accumulates in the brine beneath the buoyant current, and we account for this effect by assuming that a dense mound of brine with a uniform and constant concentration of dissolved CO_2 grows on the bottom of the aquifer as the buoyant current shrinks. The model is designed to capture: (1) the decay in dissolution flux by stopping convective dissolution locally where the dense mound fills the region beneath the buoyant current [12], and (2) the slumping of the CO_2-rich brine layer against the bottom of the aquifer [13].

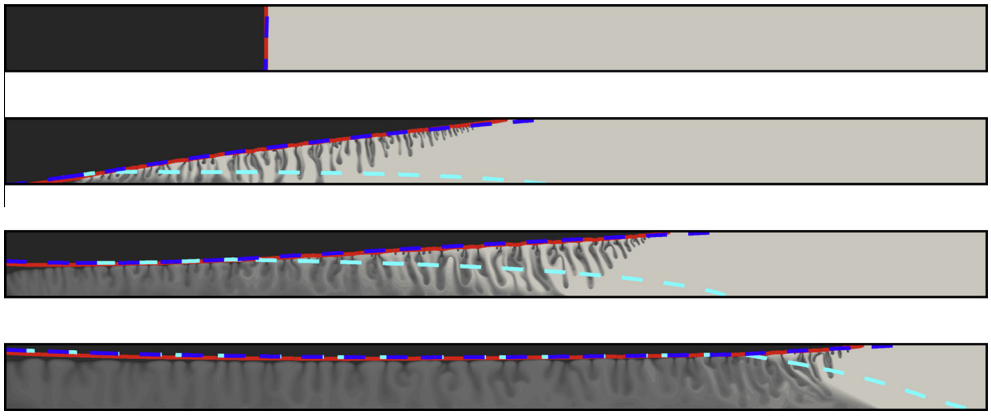

Fig. 4. The upscaled model captures the macroscopic shape of the buoyant current. Here, we compare the prediction of the upscaled model (dashed blue line) with the evolution of the neutral contour ($c = c_n = 0.56$, red line) from a high-resolution simulation for Ra = 5000, $R = 1$, and $\theta = 2.5^\circ$ at dimensionless times 0, 3, 9, and 27 (same parameters and times as in Fig. 2). Only a portion of the domain is shown ($0 \leqslant x \leqslant 15$). The concentration field (black to gray map) show the suppression of the fingering instability by the accumulation of dissolved CO_2 in the brine. We capture this in the upscaled model by disabling convective dissolution locally wherever the dense mound of brine with dissolved CO_2 (dashed cyan line) touches the buoyant current. (For interpretation of the references to color in this figure legend, the reader is referred to the web version of this article.)

The model takes the form of two coupled partial differential equations to be solved for the local thickness $h(x,t)$ of the buoyant current and the local thickness $h_d(x,t)$ of the dense mound [12,13]. We write it in dimensionless form as

$$\frac{\partial h}{\partial t} + \frac{\partial}{\partial x}\left[(1-f)h\left(N_s - N_g\frac{\partial h}{\partial x}\right) + \delta f h_d\left(N_s + N_g\frac{\partial h_d}{\partial x}\right)\right] = -\widetilde{N}_d, \quad (8)$$

$$\frac{\partial h_d}{\partial t} - \frac{\partial}{\partial x}\left[f_d h\left(N_s - N_g\frac{\partial h}{\partial x}\right) + \delta(1-f_d)h_d\left(N_s + N_g\frac{\partial h_d}{\partial x}\right)\right] = \frac{\widetilde{N}_d}{\Gamma_d}, \quad (9)$$

where x and t are defined and scaled as in Eqs. (1)–(3) and h and h_d are scaled by the aquifer thickness, L_z. The dimensionless parameters N_s, N_g, and δ measure the speed of migration due to aquifer slope relative to the speed at which the fingers fall, the speed of buoyant spreading due to gravity relative to the speed at which the fingers fall, and the migration speed of the buoyant current relative to that of the dense one, respectively. They are given by $N_s = (\Delta\rho_{gc}\mu_m \sin\theta)/(\Delta\rho_m\mu_{CO_2})$, $N_g = (\Delta\rho_{gc}\mu_m \cos\theta)/(\Delta\rho_m\mu_{CO_2})$, and $\delta = \Delta\rho_d\mu_{CO_2}/(\Delta\rho_{gc}\mu_d)$, where $\Delta\rho_{gc}$ is the amount by which the density of the brine exceeds the density of the buoyant CO_2, $\Delta\rho_d$ is the amount by which the density of the mound of brine with dissolved CO_2 exceeds the density of the ambient brine, μ_{CO_2} is the dynamic viscosity of the CO_2, μ_d is the dynamic viscosity of the dense brine with dissolved CO_2. The dissolution flux vanishes locally where the mound of brine with dissolved CO_2 fills the aquifer beneath the buoyant current:

$$\widetilde{N}_d = \begin{cases} N_d & \text{if} \quad h + h_d < 1, \\ 0 & \text{if} \quad h + h_d = 1, \end{cases} \quad (10)$$

where $N_d = q_d\mu_m/(\Delta\rho_m g k)$, and q_d is the volume of CO_2 that dissolves per unit area of CO_2–brine interface per unit time. The volume fraction Γ_d is the equivalent volume of free-phase CO_2 dissolved in one unit volume of the mound of brine with dissolved CO_2. This

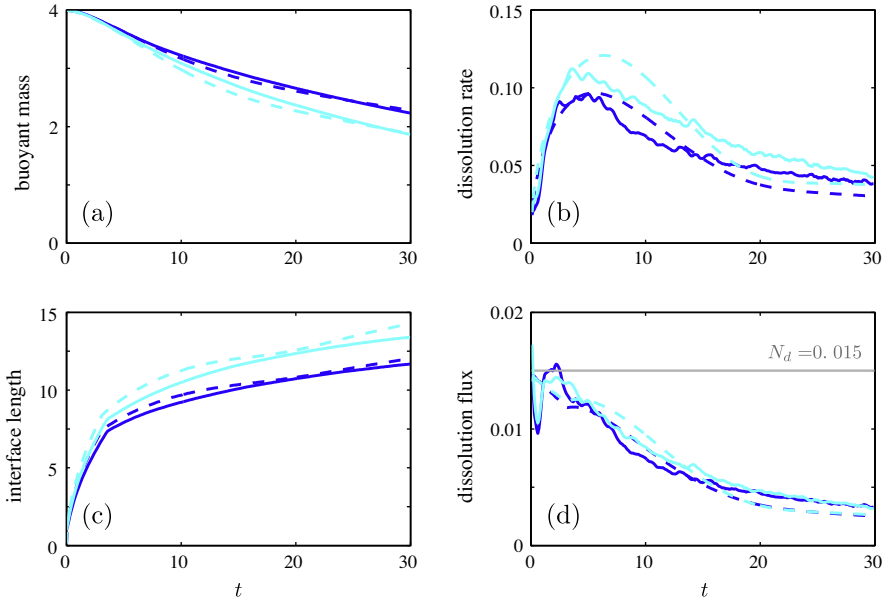

Fig. 5. The inclusion of the mound of brine with dissolved CO_2 allows the upscaled model (dashed lines) to capture the decaying average dissolution flux from the high-resolution simulations (solid lines). We again characterize the dynamics of convective dissolution via the time evolution of (a) the remaining buoyant mass, $M_b(t)$, (b) the total dissolution rate, $-dM_b/dt$, (c) the length of the CO_2–brine interface, $L(t)$, and (d) the average dissolution flux, $-(1/L)dM_b/dt$. Results shown here are for Ra = 5000, $\theta = 2.5^\circ$, and $R = 0$ (blue) and 1 (cyan). (For interpretation of the references to color in this figure legend, the reader is referred to the web version of this article.)

determines both the rate at which the dense mound grows and also the density and viscosity of the dense mound via the constitutive laws for density and viscosity. The fractional-flow functions f and f_d are given by $f(h,h_d) = \mathcal{M}h/[\mathcal{M}h + \mathcal{M}_d h_d + (1-h-h_d)]$ and $f_d(h,h_d) = h_d/[\mathcal{M}h + \mathcal{M}_d h_d + (1-h-h_d)]$, where $\mathcal{M} = \mu_{\text{brine}}/\mu_{\text{CO}_2}$ is the mobility ratio for the buoyant current (μ_{brine} is the dynamic viscosity of the brine) and $\mathcal{M}_d = \mu_{\text{brine}}/\mu_d$ is the mobility ratio for the dense mound.

All of the parameters in this upscaled model are readily derived from the parameters and constitutive laws for the full problem with the exception of the upscaled dissolution flux N_d and the volume fraction Γ_d. We measure the dissolution flux directly from our high-resolution numerical simulations, taking the dimensionless upscaled flux to be the typical average flux per unit length before the brine begins to saturate, $N_d \approx 0.015$ (Fig. 3(d)). We treat the concentration Γ_d as a fitting parameter, choosing $\Gamma_d \approx 0.18$ as a value that captures the rate at which the dissolution flux decays as the brine saturates for $Ra = 5000$ and $R = 0$. Further numerical simulations and laboratory experiments for a stationary layer and for a migrating current will be necessary to study the details of this accumulation process to develop a predictive model for the value of Γ_d. Here, we use these values of N_d and Γ_d for all comparisons (*i.e.*, $R = 0$ and $R = 1$).

We find that this upscaled model captures the evolution of the buoyant current and also the suppression of convective dissolution under the left portion of the current as dissolved CO_2 accumulates in the brine (Fig. 4). Although the dissolution flux in the upscaled model can take only one of two values locally, $\widetilde{N}_d = 0.015$ or 0 (Eq. (10)), we find that this is sufficient to capture the dynamics of the decaying average dissolution flux from the high-resolution simulations (Fig. 5).

6. Conclusions

Using high-resolution numerical simulations, we have studied the detailed dynamics of convective dissolution from a buoyant current of CO_2 in a sloping aquifer. We have found that, much like for a stationary layer of CO_2 dissolving into brine, the dissolution flux from a buoyant current is characterized by three regimes: an early-time diffusive regime before the onset of convection, an intermediate constant-flux regime, and a late-time decay as convection is suppressed by the accumulation of dissolved CO_2 in the brine. We have found, further, that these dynamics are independent of Ra for $\text{Ra} \approx 5000$ and higher (Fig. 3).

We have shown that the macroscopic evolution of the buoyant current can be captured with an upscaled, sharp-interface model that assumes a constant dissolution flux and accounts for the accumulation of dissolved CO_2 with a dense mound that grows and slumps on the bottom of the aquifer as the buoyant current shrinks and spreads (Fig. 4). The upscaled dissolution flux q_d is the essential input for upscaled models such as the ones discussed here and elsewhere [12,11,13,14]. Our high-resolution simulations allow us to obtain realistic values for this parameter in the context of a migrating current. The upscaled model also captures the smooth decay in the average dissolution flux even though we use a binary "on–off" model for the flux locally (Fig. 5). These results provide support for insights derived previously from upscaled models based on similar assumptions [12,11,13]. In addition, this provides us with a sound base for extending the upscaled model to more complex systems such as heterogeneous aquifers, which will be subject of future work.

We have assumed in the upscaled model that dissolved CO_2 accumulates in the brine as a dense mound of constant and uniform CO_2 concentration [12,13]. This concentration determines both the rate at which the dense mound grows and also the rate at which it slumps relative to the ambient brine, and is unknown *a priori*. Here, we have treated this concentration as a fitting parameter. Further high-resolution simulations for a stationary layer and for a migrating current will be necessary to study the details of this accumulation process. At later times, the slumping and down-slope migration of the dense mound will compete with mixing driven by diffusion and dispersion [42].

In our high-resolution numerical simulations, we have neglected capillarity and instead assumed that the buoyant fluid and the dense fluid are perfectly miscible, taking advantage of constitutive laws inspired by the analogue fluids that have been used to study convective dissolution in the laboratory [15,16]. This assumption will be reasonable when the capillary pressure is small relative to typical viscous and gravitational pressure changes in the flow. The impact of capillarity on the evolution of gravity currents is increasingly well understood [20,21,41,23,22]. Recent studies also suggest that capillarity can have a quantitative impact on the dissolution flux [25,41,26,27], but a complete understanding of these effects will require further study including laboratory experiments in addition to mathematical modeling and numerical simulation.

Our 2D analogue-fluid model requires a dimensionless density law and three other dimensionless parameters: the Rayleigh number; the log of the mobility ratio; and the aspect ratio of the initial condition. We discuss appropriate values of these three parameters in Section 3 above. The dimensionless density law can be characterized by two parameters: the concentration at which the density maximum occurs and the ratio of the two density differences (Fig. 1). The concentration at which the density maximum occurs plays the role of the solubility since convective dissolution will stop as the density of the ambient fluid approaches the maximum attainable density. For the analogue fluids used here, this value is $c_m = 0.26$. Appropriate values for carbon sequestration are 25 to 50 times smaller (~ 0.005–0.01 [4]). This means that the brine underlying the CO_2 would saturate with dissolved CO_2 much more quickly than in our analogue system. However, the ratio of the density difference that drives the migration of the gravity current to the one that drives convective dissolution is much smaller in the analogue system (~ 3.6) than in the field (~ 25–60 [4]). This means that a gravity current of supercritical CO_2 in the field would generally migrate faster compared to the rate at which it dissolves than in our analogue-fluid simulations, implying that the saturation of the water beneath the plume will tend to play a lesser role in the field. Similarly, the density-driven migration of the mound of water with dissolved CO_2 is likely to be much less important in the field since it migrates very slowly compared to the buoyant plume. However, both effects can be extremely important in horizontal or weakly sloping aquifers [12,13].

We have confined our modeling and simulations here to two dimensions, but three-dimensional flow effects can be important in scenarios where, for example, the lateral extent of the plume is not large compared to its length [43]. Studies of the dissolution of a stationary layer in 3D suggest a qualitatively similar evolution of flux to the one observed here [38,44]. High-resolution simulations combining migration and convective dissolution in 3D, as we have done here in 2D, would be a very interesting follow-up study.

Acknowledgments

JJH acknowledges the support from the FP7 Marie Curie Actions of the European Commission, via the CO2-MATE project (PIOF-GA-2009-253678), and the FP7 EU project PANACEA (Grant Agreement No. 282900). CWM gratefully acknowledges the support of a postdoctoral fellowship from the Yale Climate & Energy Institute. RJ

acknowledges funding by the US Department of Energy (DE-FE0009738).

Appendix A. Equations in dimensional form

Here we present the 2D mathematical model in dimensional form. We present the upscaled (1D) mathematical model in dimensional form in Appendix C.

Contrary to the rest of the paper, variables without decoration are dimensional and those with tildes are dimensionless. The equations governing incompressible fluid flow and advective–dispersive mass transport, where we adopt the Boussinesq approximation and model hydrodynamic dispersion as a Fickian process, take the form [29]

$$\nabla \cdot \mathbf{u} = 0, \tag{A.1}$$

$$\mathbf{u} = -\frac{k}{\mu(c)}(\nabla p + \rho(c) g \sin\theta \hat{\mathbf{e}}_x + \rho(c) g \cos\theta \hat{\mathbf{e}}_z), \tag{A.2}$$

$$\phi \frac{\partial c}{\partial t} = -\mathbf{u} \cdot \nabla c + \phi D_m \nabla^2 c, \tag{A.3}$$

Dimensional Eqs. (A.1)–(A.3) are related to their dimensionless counterparts Eqs. (1)–(3) by the scalings $t = (\phi \mu_m L_z / \Delta\rho_m g k)\tilde{t}$, $\nabla = \tilde{\nabla}/L_z$, $u = (\Delta\rho_m g k/\mu_m)\tilde{u}$, $p = \Delta\rho_m g L_z \tilde{p} + \rho(c=0)gz + p_0$, $\mu = \mu_m \tilde{\mu}$, and $\rho = \Delta\rho_m \tilde{\rho} + \rho_0$. p_0 and ρ_0 are a dimensional reference pressure and dimensional brine density, respectively.

The density difference $\rho(c = c_m) - \rho(c = 0) = \Delta\rho_m$ drives convective dissolution, while the density difference $\rho(c = 0) - \rho(c = 1) = \Delta\rho_{gc}$ drives the migration of the gravity current.

Appendix B. Convergence analysis

Fingering instabilities are very sensitive to numerical discretization [45]. To accurately capture the dynamics of convective dissolution, it is essential for our simulations to resolve the smallest relevant length and time scales. The smallest such length scale for convective dissolution is believed to be the critical wavelength for the onset of convection, $\lambda_c \approx 90 L_z/\mathrm{Ra}$ [9]. We present results here for Ra as high as 10,000 (Fig. 3), for which $\lambda_c/L_z \approx 0.009$. Larger values of Ra require proportionally finer spatial discretizations. Allocating at least two horizontal grid blocks per wavelength then suggests a minimum horizontal resolution of ~ 220 grid blocks per unit dimensionless length for Ra = 10000. We use 500 grid blocks per unit length in both directions (10000×500 for a domain of 20×1) for all simulations, which we expect to be sufficient.

Regarding the convergence of macroscopic quantities such as the dissolution flux, we choose a discretization for which the results vary by a few percent or less when the grid is refined further. We perform such a convergence analysis by comparing a sequence of simulations performed on meshes of increasing resolution. We compare resolutions of 200–600 grid blocks per unit dimensionless length (same in the horizontal and vertical directions). Since the dimensionless height of the domain is always 1, the resolution is the same as the number of grid blocks N_z in the vertical direction. We illustrate this convergence quantitatively in Fig. B.6 for $\mathrm{Ra} = 5000, R = 0, \theta = 0$ and a dimensionless initial width of 0.5. The domain has aspect ratio $A = 5$, so the finest mesh has 3000×600 grid blocks ($N_z = 600$). We illustrate this convergence

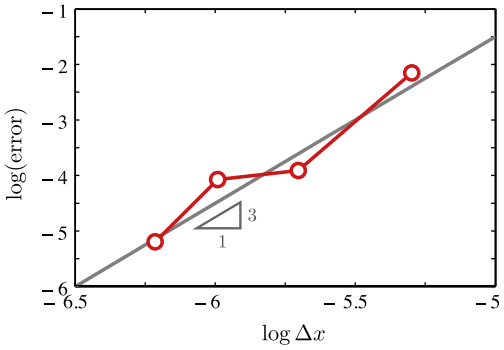

Fig. B.6. Numerical convergence of macroscopic quantities with grid size. Here we calculate the error in buoyant mass for grid size Δx as the log of the maximum difference between the value for that grid size and the next coarser one, $\log(\max|M_b^{k+1}(t) - M_b^k(t)|)$. These results are for $R = 0$, $\theta = 0^\circ$, and $\mathrm{Ra} = 5000$.

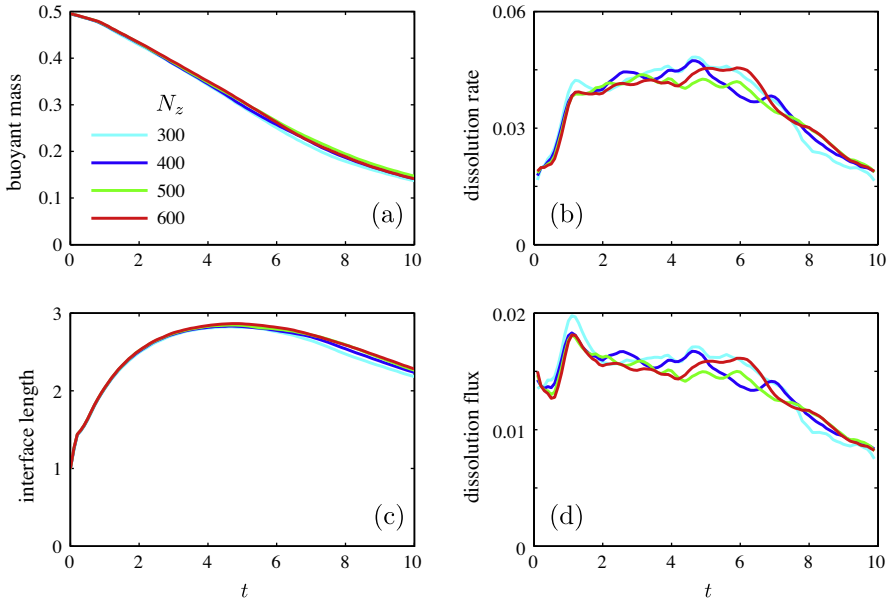

Fig. B.7. Convergence with grid size of (a) buoyant mass, (b) total dissolution rate, (c) interface length (length of the neutral contour), and (d) dissolution flux for $\mathrm{Ra} = 5000$, $R = 0$, $\theta = 0^\circ$, and a dimensionless initial width of 0.5. These macroscopic quantities converge to within a few percent for $N_z \geqslant 500$.

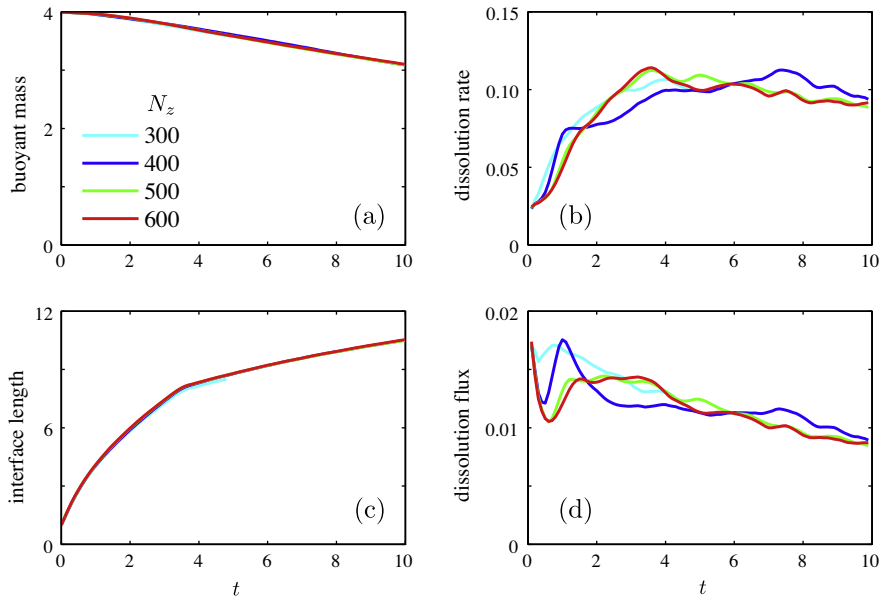

Fig. B.8. Convergence with grid size of (a) buoyant mass, (b) total dissolution rate, (c) interface length (length of the neutral contour), and (d) dissolution flux for Ra = 5000, $R = 1$, $\theta = 2.5^\circ$, aspect ratio $A = 20$, and a dimensionless initial width of 4. As for $R = 0$, these quantities converge to within a few percent for $N_z \geqslant 500$.

qualitatively in Figs. B.7 and B.8 for $R = 0$ and $R = 1$, respectively. Based on these results, we choose a resolution of 500 grid blocks per unit length for all simulations presented here as a compromise between numerical accuracy and computational burden. We expect other parameters, such as the slope or the shape of the density curve, to have little impact on convergence.

Appendix C. Derivation of the upscaled model

Here we briefly outline the derivation of the upscaled (1D) model in dimensional form. This model is an extension of the model of [12] to include the density-driven slumping of the dense CO_2-rich brine layer against the bottom of the aquifer as in [13], but without residual fluids. The model may also be viewed as an extension of the model of [13] to include slope and a net background flow. We refer the reader to these previous works for a detailed discussion and justification of the main assumptions, which include vertical-flow equilibrium and the sharp-interface approximation. Here, as in Appendix A and contrary to the rest of the paper, all quantities are *dimensional*.

We assume that the fluids are vertically segregated into three regions of uniform density and viscosity, and that these regions are separated by sharp interfaces. The three regions contain free-phase CO_2, brine, and brine with a volume fraction Γ_d of dissolved CO_2. At position x and time t, these regions have respective thicknesses $h(x,t), h_w(x,t)$, and $h_d(x,t)$, where $h + h_w + h_d = L_z$. The CO_2 has density ρ_g and viscosity μ_g; the brine has density ρ_w and viscosity μ_w; and the brine with dissolved CO_2 has density ρ_d and viscosity μ_d.

We write the Darcy velocity of the fluid in each region as

$$\mathbf{u}_g = -\frac{k}{\mu_g}\left(\nabla p_g + \rho_g g \sin\theta \hat{\mathbf{e}}_x + \rho_g g \cos\theta \hat{\mathbf{e}}_z\right), \tag{C.1}$$

$$\mathbf{u}_w = -\frac{k}{\mu_w}(\nabla p_w + \rho_w g \sin\theta \hat{\mathbf{e}}_x + \rho_w g \cos\theta \hat{\mathbf{e}}_z), \tag{C.2}$$

$$\mathbf{u}_d = -\frac{k}{\mu_d}(\nabla p_d + \rho_d g \sin\theta \hat{\mathbf{e}}_x + \rho_d g \cos\theta \hat{\mathbf{e}}_z), \tag{C.3}$$

where p_g, p_w, and p_d are the fluid pressures in each region. We next assume vertical-flow equilibrium, neglecting the vertical component of the fluid velocity relative to the horizontal one because of the characteristic long and thin nature of the flow. The z-components of Eqs. (C.1)–(C.3) then imply that the pressure distribution in each region is hydrostatic and given by

$$p_g = p_i(x,t) + \rho_g g \cos\theta (L_z - h - z), \tag{C.4}$$

$$p_w = p_i(x,t) + \rho_w g \cos\theta (L_z - h - z), \tag{C.5}$$

$$p_d = p_i(x,t) + \rho_w g \cos\theta h_w + \rho_d g \cos\theta (h_d - z), \tag{C.6}$$

where $p_i(x,t)$ is the unknown pressure along the CO_2 interface ($z = L_z - h$). Substituting Eqs. (C.4)–(C.6) into the x-components of Eqs. (C.1)–(C.3) gives expressions for the horizontal fluid velocity in each region in terms of p_i.

Since we have taken the fluids and the rock to be incompressible, the total volume of fluid flowing through any cross-section of the aquifer must be conserved. This requirement can be written

$$(\mathbf{u}_g \cdot \hat{\mathbf{e}}_x)h + (\mathbf{u}_w \cdot \hat{\mathbf{e}}_x)h_w + (\mathbf{u}_d \cdot \hat{\mathbf{e}}_x)h_d = Q, \tag{C.7}$$

where the constant total volume flow rate Q may be nonzero when there is fluid injection or extraction, leakage, or if there is a natural groundwater through-flow. Eq. (C.7) can be combined with the expressions for the horizontal fluid velocity obtained from Eqs. (C.1)–(C.3) and (C.4)–(C.6) to eliminate the unknown pressure p_i.

Finally, local volume conservation dictates that the change in the thickness of each region must be balanced locally by the divergence of the flux of fluid through that region and the transfer of volume from one region to another. This requirement can be written

$$\phi\frac{\partial h}{\partial t} + \frac{\partial}{\partial x}\left[(\mathbf{u}_g \cdot \hat{\mathbf{e}}_x)h\right] = -\widetilde{q}_d, \tag{C.8}$$

$$\phi\frac{\partial h_d}{\partial t} + \frac{\partial}{\partial x}\left[(\mathbf{u}_d \cdot \hat{\mathbf{e}}_x)h_d\right] = \frac{\widetilde{q}_d}{\Gamma_d}, \tag{C.9}$$

where $\widetilde{q}_d$ is defined by

$$\widetilde{q}_d = \begin{cases} q_d & \text{if} \quad h + h_d < L_z, \\ 0 & \text{if} \quad h + h_d = L_z \end{cases} \tag{C.10}$$

and q_d is the flux due to convective dissolution, which transfers volume from the CO_2-region to the region of brine with dissolved CO_2. Combining all of the above and eliminating h_w through the require-

ment that the three thicknesses sum to the total thickness of the aquifer, the resulting model is given by

$$\frac{\partial h}{\partial t}+\frac{Q}{\phi}\frac{\partial f}{\partial x}+\frac{\Delta\rho_{gc}gk}{\phi\mu_g}\frac{\partial}{\partial x}\left[\sin\theta(1-f)h-\cos\theta(1-f)h\frac{\partial h}{\partial x}\right]+\frac{\Delta\rho_d gk}{\phi\mu_d}\frac{\partial}{\partial x}\left[\sin\theta f h_d+\cos\theta f h_d\frac{\partial h_d}{\partial x}\right]=-\widetilde{q}_d/\phi, \quad (C.11)$$

$$\frac{\partial h_d}{\partial t}+\frac{Q}{\phi}\frac{\partial f_d}{\partial x}+\frac{\Delta\rho_{gc}gk}{\phi\mu_g}\frac{\partial}{\partial x}\left[-\sin\theta f_d h+\cos\theta f_d h\frac{\partial h}{\partial x}\right]+\frac{\Delta\rho_d gk}{\phi\mu_d}\frac{\partial}{\partial x}\left[-\sin\theta(1-f_d)h_d-\cos\theta(1-f_d)h_d\frac{\partial h_d}{\partial x}\right]=\frac{\widetilde{q}_d}{\phi\Gamma_d}, \quad (C.12)$$

where $f(h,h_d)$ and $f_d(h,h_d)$ are as defined in Section 5. Eqs. (C.11) and (C.12) are related to their dimensionless counterparts Eqs. (8) and (9) by scaling h and h_d with characteristic thickness L_z, x with characteristic length L_z, and t with characteristic time $\phi\mu_m L_z/\Delta\rho_m gk$. Note that we have taken $Q=0$ in Eqs. (8) and (9) for comparison with our 2D results, in which there is no net flow.

References

[1] Bachu S, Gunter WD, Perkins EH. Aquifer disposal of CO_2: hydrodynamic and mineral trapping. Energy Convers Manage 1994;35:269–79. http://dx.doi.org/10.1016/0196-8904(94)90060-4.

[2] Lackner KS. Climate change: a guide to CO_2 sequestration. Science 2003;300:1677–8. http://dx.doi.org/10.1126/science.1079033.

[3] Orr Jr FM. Onshore geologic storage of CO_2. Science 2009;325:1656–8. http://dx.doi.org/10.1126/science.1175677.

[4] Szulczewski ML, MacMinn CW, Herzog HJ, Juanes R. Lifetime of carbon capture and storage as a climate-change mitigation technology. Proc Natl Acad Sci 2012;109:5185–9. http://dx.doi.org/10.1073/pnas.1115347109.

[5] IPCC, Carbon dioxide capture and storage. Special report prepared by working group III of the intergovernmental panel on climate change, Cambridge, UK; 2005. (ISBN 13-978-0-521-86643-9).

[6] Weir GJ, White SP, Kissling WM. Reservoir storage and containment of greenhouse gases. Transp Porous Media 1996;23:37–60. http://dx.doi.org/10.1016/0196-8904(95)00060-Q.

[7] Lindeberg E, Wessel-Berg D. Vertical convection in an aquifer column under a gas cap of CO_2. Energy Convers Manage 1997;38:S229–34. http://dx.doi.org/10.1016/S0196-8904(96)00274-9.

[8] Ennis-King J, Preston I, Paterson L. Onset of convection in anisotropic porous media subject to a rapid change in boundary conditions. Phys Fluids 2005;17:084107. http://dx.doi.org/10.1063/1.2033911.

[9] Riaz A, Hesse M, Tchelepi HA, Orr Jr FM. Onset of convection in a gravitationally unstable diffusive boundary layer in porous media. J Fluid Mech 2006;548:87–111. http://dx.doi.org/10.1017/S0022112005007494.

[10] Pruess K, Nordbotten J. Numerical simulation studies of the long-term evolution of a CO_2 plume in a saline aquifer with a sloping caprock. Transp Porous Media 2011;90:135–51. http://dx.doi.org/10.1007/s11242-011-9729-6. http://dx.doi.org/.

[11] Gasda SE, Nordbotten JM, Celia MA. Vertically-averaged approaches for CO_2 migration with solubility trapping. Water Resour Res 2011;47:W05528. http://dx.doi.org/10.1029/2010WR009075.

[12] MacMinn CW, Szulczewski ML, Juanes R. CO2 migration in saline aquifers. Part 2: Capillary and solubility trapping. J Fluid Mech 2011;688:321–51. http://dx.doi.org/10.1017/jfm.2011.379.

[13] MacMinn CW, Neufeld JA, Hesse MA, Huppert HE. Spreading and convective dissolution of carbon dioxide in vertically confined, horizontal aquifers. Water Resour Res 2012;48:W11516. http://dx.doi.org/10.1029/2012WR012286.

[14] MacMinn CW, Juanes R. Buoyant currents arrested by convective dissolution. Geophys Res Lett 2013;40:2017–22. http://dx.doi.org/10.1002/grl.50473.

[15] Neufeld JA, Hesse MA, Riaz A, Hallworth MA, Tchelepi HA, Huppert HE. Convective dissolution of carbon dioxide in saline aquifers. Geophys Res Lett 2010;37:L22404. http://dx.doi.org/10.1029/2010GL044728.

[16] Backhaus S, Turitsyn K, Ecke RE. Convective instability and mass transport of diffusion layers in a Hele-Shaw geometry. Phys Rev Lett 2011;106:104501. http://dx.doi.org/10.1103/PhysRevLett.106.104501.

[17] Juanes R, Spiteri EJ, Orr FM, Blunt MJ. Impact of relative permeability hysteresis on geological CO_2 storage. Water Resour Res 2006;42(12):W12418. http://dx.doi.org/10.1029/2005WR004806.

[18] Hesse MA, Orr Jr FM, Tchelepi HA. Gravity currents with residual trapping. J Fluid Mech 2008;611:35–60. http://dx.doi.org/10.1017/S002211200800219X.

[19] MacMinn CW, Szulczewski ML, Juanes R. CO2 migration in saline aquifers. Part 1: Capillary trapping under slope and groundwater flow. J Fluid Mech 2010;662:329–51. http://dx.doi.org/10.1017/S0022112010003319.

[20] Nordbotten JM, Dahle HK. Impact of the capillary fringe in vertically integrated models for CO_2 storage. Water Resour Res 2011;47:W02537. http://dx.doi.org/10.1029/2009WR008958.

[21] Golding MJ, Neufeld JA, Hesse MA, Huppert HE. Two-phase gravity currents in porous media. J Fluid Mech 2011;678:248–70. http://dx.doi.org/10.1017/jfm.2011.110.

[22] Golding MJ, Huppert HE, Neufeld JA. The effects of capillary forces on the axisymmetric propagation of two-phase, constant-flux gravity currents in porous media. Phys Fluids 2013;25:036602. http://dx.doi.org/10.1063/1.4793748.

[23] Zhao B, MacMinn CW, Szulczewski ML, Neufeld JA, Huppert HE, Juanes R. Interface pinning of immiscible exchange flows in porous media. Phys Rev E 2013;87:023015. http://dx.doi.org/10.1103/PhysRevE.87.023015.

[24] Doster F, Nordbotten JM, Celia MA. Impact of capillary hysteresis and trapping on vertically integrated models for CO_2 storage. Adv Water Resour 2013;62:465–74. http://dx.doi.org/10.1016/j.advwatres.2013.09.005.

[25] Elenius MT, Nordbotten JM, Kalisch H. Effects of a capillary transition zone on the stability of a diffusive boundary layer. IMA J Appl Math 2012;77(6):771–87. http://dx.doi.org/10.1093/imamat/hxs054.

[26] Hewitt DR, Neufeld JA, Lister JR. Convective shutdown in a porous medium at high Rayleigh number. J Fluid Mech 2013;719:551–86. http://dx.doi.org/10.1017/jfm.2013.23.

[27] Li B, Tchelepi HA, Benson SM. Influence of capillary entry pressure on CO_2 solubility trapping. Adv Water Resour 2013;62:488–98. http://dx.doi.org/10.1016/j.advwatres.2013.08.005.

[28] Nicot J-P. Evaluation of large-scale CO_2 storage on fresh-water sections of aquifers: an example from the Texas Gulf Coast Basin. Int J Greenhouse Gas Control 2008;2:582–93. http://dx.doi.org/10.1016/j.ijggc.2008.03.004.

[29] Ruith M, Meiburg E. Miscible rectilinear displacements with gravity override. Part 1: Homogeneous porous medium. J Fluid Mech 2000;420:225–57. http://dx.doi.org/10.1017/S0022112000001543.

[30] Hidalgo JJ, Carrera J. Effect of dispersion on the onset of convection during CO_2 sequestration. J Fluid Mech 2009;640:441–52. http://dx.doi.org/10.1017/S0022112009991480.

[31] Juanes R, MacMinn CW, Szulczewski ML. The footprint of the CO_2 plume during carbon dioxide storage in saline aquifers: storage efficiency for capillary trapping at the basin scale. Transp Porous Media 2010;82:19–30. http://dx.doi.org/10.1007/s11242-009-9420-3.

[32] Hidalgo JJ, Fe J, Cueto-Felgueroso L, Juanes R. Scaling of convective mixing in porous media. Phys Rev Lett 2012;109:264503. http://dx.doi.org/10.1103/PhysRevLett.109.264503.

[33] Wilson EJ, Friedmann SJ, Pollak MF. Research for deployment: incorporating risk, regulation, and liability for carbon capture and sequestration. Environ Sci Technol 2007;41:5945–52. http://dx.doi.org/10.1021/es062272t.

[34] Seto CJ, McRae GJ. Reducing risk in basin scale CO_2 sequestration: a framework for integrated monitoring design. Environ Sci Technol 2011;45:845–59. http://dx.doi.org/10.1021/es102240w.

[35] Slim AC, Bandi MM, Miller JC, Mahadevan L. Dissolution-driven convection in a Hele-Shaw cell. Phys Fluids 2013;25:024101. http://dx.doi.org/10.1063/1.4790511.

[36] Huppert HE, Woods AW. Gravity-driven flows in porous layers. J Fluid Mech 1995;292:55–69. http://dx.doi.org/10.1017/S0022112095001431.

[37] Hesse MA, Tchelepi HA, Cantwell BJ, Orr Jr FM. Gravity currents in horizontal porous layers: transition from early to late self-similarity. J Fluid Mech 2007;577:363–83. http://dx.doi.org/10.1017/S0022112007004685.

[38] Pau GSH, Bell JB, Pruess K, Almgren AS, Lijewski MJ, Zhang K. High-resolution simulation and characterization of density-driven flow in CO_2 storage in saline aquifers. Adv Water Resour 2010;33:443–55. http://dx.doi.org/10.1016/j.advwatres.2010.01.009.

[39] Lyle S, Huppert HE, Hallworth M, Bickle M, Chadwick A. Axisymmetric gravity currents in a porous medium. J Fluid Mech 2005;543:293–302. http://dx.doi.org/10.1017/S0022112005006713.

[40] Nordbotten JM, Celia MA. Similarity solutions for fluid injection into confined aquifers. J Fluid Mech 2006;561:307–27. http://dx.doi.org/10.1017/S0022112006000802.

[41] Gasda SE, Nordbotten JM, Celia MA. Application of simplified models to CO_2 migration and immobilization in large-scale geological systems. Int J Greenhouse Gas Control 2012;9:72–84. http://dx.doi.org/10.1016/j.ijggc.2012.03.001.

[42] Szulczewski ML, Juanes R. The evolution of miscible gravity currents in horizontal porous layers. J Fluid Mech. http://dx.doi.org/10.1017/jfm.2012.631.

[43] Nordbotten JM, Flemisch B, Gasda SE, Nilsen HM, Fan Y, Pickup GE, Wiese B, Celia MA, Dahle HK, Eigestad GT, Pruess K. Uncertainties in practical simulation of CO_2 storage. Int J Greenhouse Gas Control 2012;9:234–42. http://dx.doi.org/10.1016/j.ijggc.2012.03.007.

[44] Fu X, Cueto-Felgueroso L, Juanes R. Pattern formation and coarsening dynamics in three-dimensional convective mixing in porous media. Philos Trans R Soc A (in press).

[45] Schincariol RA, Schwartz FW, Mendoza CA. On the generation of instabilities in variable density flow. Water Resour Res 1994;30:913–27. http://dx.doi.org/10.1029/93WR02951.